

Integrated Bioelectronic Proton-Gated Logic Elements Utilizing Nanoscale Patterned Nafion – Supplementary Information

J.G. Gluschke¹, J. Seidl¹, R.W. Lyttleton^{1, 2}, K. Nguyen¹, M. Lagier¹, F. Meyer¹, P. Krogstrup³, J. Nygård³, S. Lehmann², A.B. Mostert⁴, P. Meredith^{5,6} & A.P. Micolich^{1,*}

¹ *School of Physics, University of New South Wales, Sydney NSW 2052, Australia*

² *NanoLund, Lund University, SE-221 00 Lund, Sweden*

³ *Center for Quantum Devices and Station Q Copenhagen, University of Copenhagen, DK-2100 Copenhagen, Denmark*

⁴ *Chemistry Department, Swansea University, Swansea SA2 8PP, Wales, U.K.*

⁵ *Physics Department, Swansea University, Swansea SA2 8PP, Wales, U.K.*

⁶ *School of Mathematics and Physics, University of Queensland, Brisbane, QLD 4072, Australia*

* Corresponding author email: adam.micolich@nanoelectronics.physics.unsw.edu.au

Mechanisms for generating solubility contrast in Nafion films by electron-beam exposure

An interesting question related to our study is what the mechanism is for generating solubility contrast in Nafion films by electron-beam exposure. Two obvious candidates come to mind: a) chemical changes in the Nafion, e.g., cross-linking, arising from injection of energetic electrons by the beam, and b) structural changes in the Nafion arising from, e.g., localised heating generated by the energy dissipated by the beam impacting the substrate.

The following two sections describe two studies we performed to identify the extent that these may contribute to the patterning we describe in the main text. They are a prelude to a longer, more detailed study of electron-beam patterned Nafion that we will publish as a separate work.

X-ray photoelectron spectroscopy on EBL-patterned Nafion thin films

We begin by looking at chemical changes since they are the most obvious possibility given how most resist technologies work in the device fabrication industry. To do this we performed x-ray photoelectron spectroscopy (XPS) on electron-beam exposed and pristine Nafion films prepared as follows.

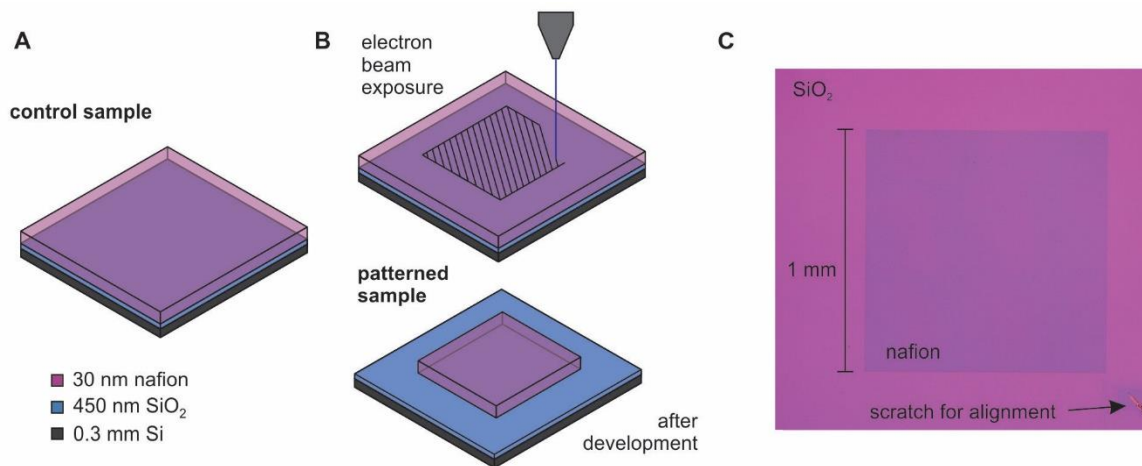


Figure S1. (A) Diagram of the control sample for XPS. (B) Diagram of the EBL-patterned sample for XPS. (C) Optical microscopy image of the EBL-patterned sample after development.

The samples were prepared as ~30 nm Nafion films on Si/SiO₂ substrates by spin-coating at 3500 rpm for 60 s with a ramp of 1000 rpm/s. The first sample was measured with no further processing as a control (see Figure S1A). On the second sample (see Figure S1B), we exposed a $1 \times 1 \text{ mm}^2$ square to a 10 kV electron-beam with current 230 pA to a dose of $9 \mu\text{C}/\text{cm}^2$. The second sample was then developed in 1:1 2-propanol:acetone for 60 s leaving only the exposed area. Figure S1C shows an optical microscopy image of the patterned Nafion sample. A scratch in the substrate was used to optically align the x-ray beam with the patterned Nafion area for the XPS study. The XPS measurement of the patterned sample still detected a small Si signature (see below) suggesting slight over-illumination of the Nafion area producing a contribution from the SiO₂ substrate. We correct for this substrate contribution in the analysis that follows.

XPS was performed with an ESCALAB250Xi X-ray photoelectron spectrometer (Thermo Scientific) with a mono-chromated Al K α source (energy 1486.68 eV). A beam with 500 μm spot size, 90° photoelectron take-off angle and 120 W power (13.8 kV \times 8.7 mA) was used. Survey and high-resolution scans were obtained at 100 eV and 20 eV pass energies respectively. Data analysis of the XPS spectra was performed using Shirley background curves for the high-resolution scans. Peaks were modelled using pseudo-Voigtians with 30% Lorentzian character.

Peak assignment was done in accordance with previously published modelling of expected XPS parameters and data on Nafion¹ and Fomblin Y.² Figure S2 shows a sketch of the chemical structure of Nafion. The assigned peak numbers in our fits for the carbon (green) and oxygen (blue) high resolution scans are labelled to their corresponding atoms in the structure.

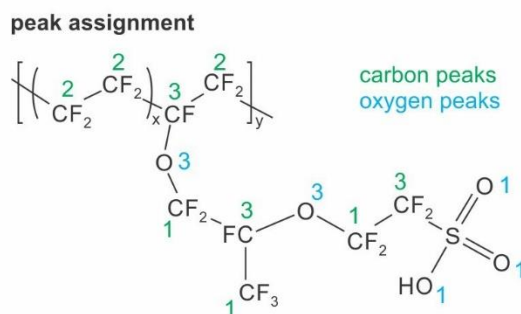


Figure S2. The chemical structure of Nafion. Fitted peaks in the C and O XPS spectra were attributed to C and O atoms as indicated in this Figure. Green/blue numbers correspond to carbon/oxygen peaks, with the same numbering used in Figure S5 and S6.

Initial analysis of the Nafion control and EBL samples gave atomic ratios commensurate with expectations for Nafion-117 (see Table S1), i.e. roughly 14 CF₂ units on the backbone before a sulfonated pendant group.³ This data indicates that no proportional atomic loss of the material has occurred during EBL processing. Thus, any chemical changes arising in the EBL process are due to chemical rearrangement rather than species loss.

Table S1. Atomic percentages *at%* of the atoms expected from Nafion. For the control and EBL samples we have subtracted out the contribution from N and Si peaks indicating impurities. Atomic ratios of the samples are the same as the ideal within a 10% relative uncertainty on all the values except for sulfur.

Nafion	Sulfur <i>at%</i>	Oxygen <i>at%</i>	Carbon <i>at%</i>	Fluorine <i>at%</i>	Total <i>at%</i>
Ideal	1.5	7.4	30.9	60.3	100
Control	1.1	7.1	27.6	64.2	100
EBL	1.0	6.6	29.5	62.9	100

A small amount of nitrogen was detected at comparable levels to sulphur in the survey scans of both the control and EBL samples. The nitrogen is assigned as an impurity in both cases. In the detailed scans, we first turn to the fluorine peaks (Figure S3). There is little change in the F peaks indicating that the fluorine chemistry is unchanged, i.e., all F remains as C-F.

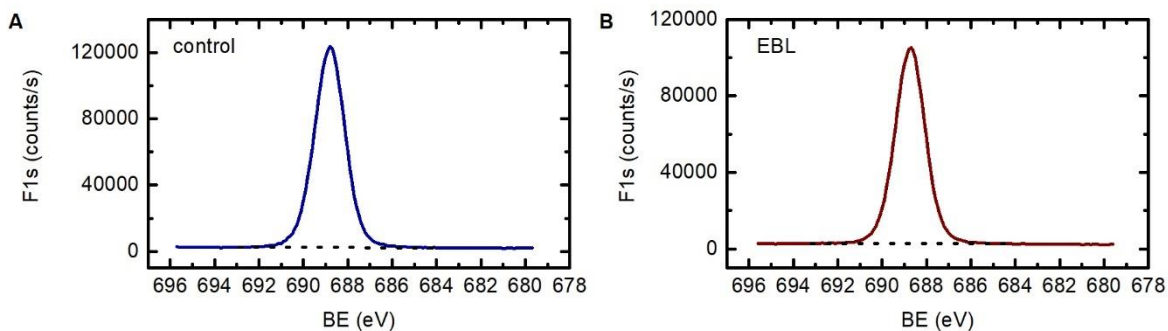


Figure S3. F1s peak vs binding energy (BE) for (A) the control sample and (B) the EBL-patterned sample. The Shirley background is presented as a black dotted line.

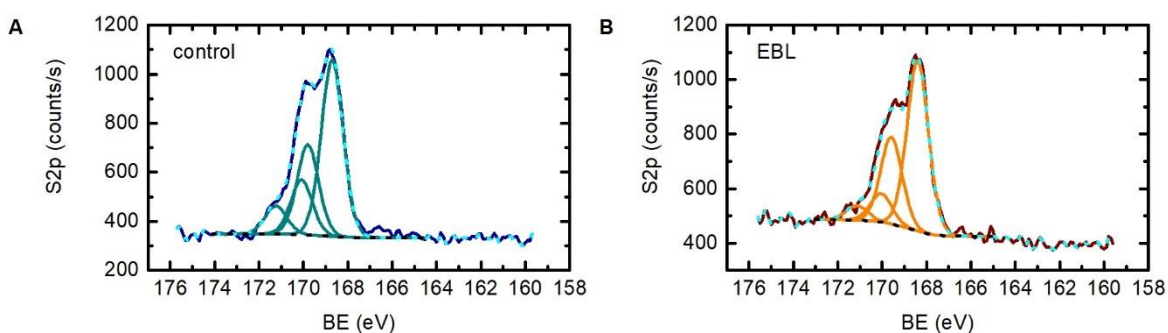


Figure S4. S2p peaks for the (A) control and (B) EBL sample. For (A) the raw data is in blue and fits in cyan. For (B) the raw data is in red and fits in orange. The light blue dotted line in both indicates the cumulative fit curve. The Shirley background is presented as a black dotted line.

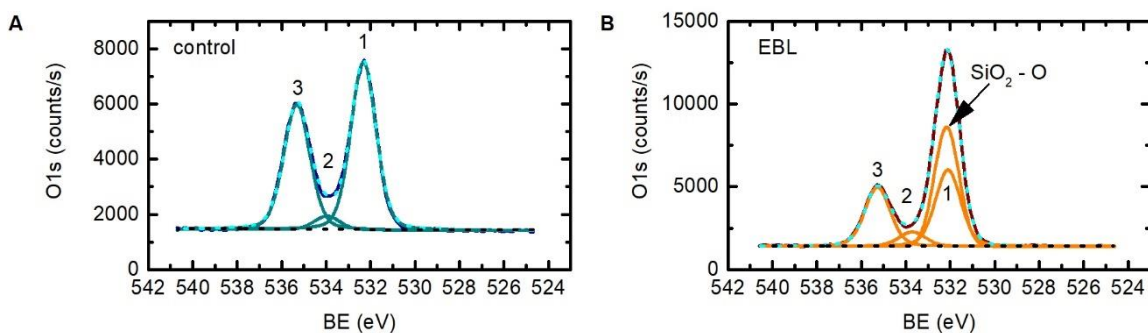


Figure S5. O1s peaks for the (A) control and (B) EBL sample. For (A) the raw data is in blue and fits in cyan. For (B) the raw data is in red and fits in orange. The light blue dotted line indicates the cumulative fit curve. The Shirley background is presented as a black dotted line. Part of Peak 1 in (B) is attributed to the exposed SiO₂ substrate generating signal via slight over-illumination.

The sulfur peaks in Figure S4 are also very similar between samples. Both peaks comport with previously published XPS data for Nafion and are consistent with a sulfonated sulphur moiety.⁴ Indeed, the corresponding sulfonated oxygen peak (Peak 1 in Figure S5) does not change after the EBL process after correcting for the SiO₂ contribution for the EBL sample (for corresponding

width and *at%*, see Tables S2 – S4). The subsequent areas in Tables S2 and 3 are what was obtained from the fits, but the *at%* value was renormalised to exclude the SiO₂ oxygen peak.

Table S2. Summary of the results of the fits (relative to the baseline) for the oxygen peaks of the control sample in Figure S5A. The sulfonated oxygen peak was fixed allowing the relative shift of the other peaks to be determined for comparison with the EBL sample.

Peak	1	2	3
BE (eV)	532.32	534.0 ± 0.2	535.32 ± 0.01
BE relative to Peak 1 [BE _{erp}] (eV)	0	-1.7 ± 0.2	-3.00 ± 0.01
Area (arb.)	9640 ± 60	800 ± 100	7410 ± 90
Atom Assignment	S- <u>O</u> (sulfonate oxygen)	Impurity (possibly N _x O _y)	C- <u>O</u> -C (ether oxygen)
<i>at%</i>	54.0 ± 0.8	4.5 ± 0.6	41.5 ± 0.8
Predicted <i>at%</i>	60	0	40
Width (eV)	1.345 ± 0.008	1.4 ± 0.1	1.39 ± 0.01

Table S3. Summary of the results of the fits (relative to the baseline) for the oxygen peaks in the EBL sample in Figure S5B. The sulfonated oxygen peak was fixed as well as the width of the oxygen impurity, which should not change. For the atomic percentages (*at%*), the oxygen contribution from the SiO₂ (Peak SiO₂ - O) was subtracted to enable direct comparison with the control sample. The predicted *at%* are the values obtained from the control sample.

Peak	1	SiO ₂ - O	2	3
BE (eV)	532.1	532.16 ± 0.02	533.7 ± 0.1	535.27 ± 0.02
BE relative to Peak 1 [BE _{erp}] (eV)	0	0.06 ± 0.02	-1.6 ± 0.1	-3.17 ± 0.02
Area (arb.)	7300 ± 400	10000 ± 500	1430 ± 90	5600 ± 100
Atom Assignment	S-O	SiO ₂	Impurity (possibly N _x O _y)	C-O-?
<i>at%</i> (with SiO ₂ excluded)	51 ± 3	N/A	10.0 ± 0.8	39 ± 2
Predicted <i>at%</i>	54.0	N/A	4.5	41.5
Width (eV)	1.345	1.300 ± 0.006	1.4	1.34 ± 0.02

Table S4. The difference between the various peak parameters of the control and EBL samples in Tables S2 and S3. Data indicates a difference between the ether peaks of the two samples.

Peak	S-O	Oxygen impurity	-O- / ether
ΔBE_{rp} (eV)	-	0.1 ± 0.3	0.17 ± 0.03
$\Delta at\%$	3 ± 4	6 ± 1	3 ± 3
$\Delta Width$ (eV)	-	-	0.05 ± 0.03

We attribute Peak 3 in the oxygen spectra in Figure S5 to the ether (-O-) groups in the side chain. This peak is a key point of difference between the control and EBL sample suggesting it may be the site of chemical action by the electron beam. To better quantify this, Tables S2 and S3 present the fit parameters for the peaks in the oxygen spectra in Figure S5A B. Table S4 focuses on the differences in peak parameters between the two samples. The tabulated data points strongly to a significant change in the ether bonds in the EBL process. The SiO₂ signal adds complexity to this analysis however, so we explore this further by turning to the carbon peak data in Figure S6.

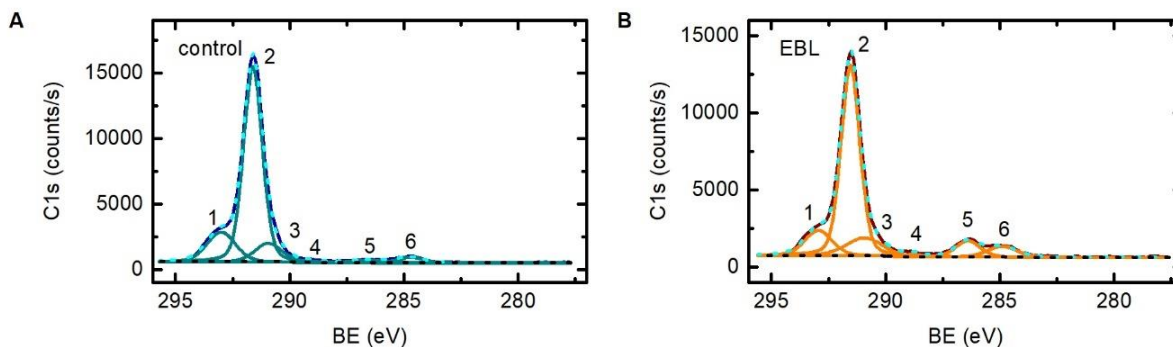


Figure S6. C1s peaks for the (A) control and (B) EBL sample. For (A) the raw data is in blue and fits in cyan. For (B) the raw data is in red and fits in orange. The light blue dotted line indicates the cumulative fit curve. The Shirley background is presented as a black dotted line.

The C1s spectra in Figure S6 show 6 separate peaks corresponding to several moieties, some of which are indicated in the chemical structure in Figure S2 (Peaks 1-3), all are denoted in Tables S5 and S6 where the fit parameters for the various peaks are presented. Table S7 presents the differences in peak parameters between the two samples. The data suggests that the carbon-oxygen bond between the carbon in a CF₂ group and its immediately adjacent oxygen in the ether is cleaved leading to a decrease in the area under Peak 1 in Figure S6. This is consistent with the observations reported by Hobson *et al.*⁵ from IR reflectance on electron-beam exposed Nafion membranes. This bond cleavage causes a slight change in the chemistry of the CF moieties still attached to oxygen, which is captured by the broadening of Peak 3 in Figure S6B, and hence indicates a diversification of the kinds of CF moieties bonded to ethers.

The CF₂ carbons lost from Peak 1 in Figure S6A appear as unsaturated, partially fluorinated carbon bonds in Peak 5 of Figure S6B, e.g., these carbons form double bonds, but what they bond to and where is not presently clear. We offer two potential scenarios. The first scenario is that the cleaved CF₂ carbon forms a double bond with its adjacent carbon (see Figure S2 for context). This implies a complete cleavage of the sidechain. The second scenario is that the CF₂ carbon forms a double

bond with another carbon elsewhere, e.g., the Nafion backbone, to produce crosslinking. The other peaks do not change much leading us to believe the first scenario is more likely. At first sight, cleavage as opposed to crosslinking could lead a reader to conclude that EBL increases solubility in contrast to our observed experimental outcome. However, Nafion is essentially a polytetrafluoroethylene (PTFE) backbone, which is insoluble, with attached pendants with sulfonate end-groups. These pendants increase the solubility of the PTFE backbone, enabling us to dissolve and spin-coat the Nafion film. By cleaving these pendants off the Nafion backbone, the solubility will decrease producing the pattern contrast we observe.

Table S5. Summary of the results of the fits (relative to the baseline) for the carbon peaks of the control sample in Figure S6A. The CF₂ peak was fixed allowing the relative shift of the other peaks to be determined for comparison with the EBL sample. The carbons in bold underline are the assigned carbons for that particular peak.

Peak	1	2	3	4	5	6
BE (eV)	293.00±0.02	291.61	290.9±0.1	289±1	286.5±0.4	284.7±0.2
BE relative to peak 2 [BE_{rp}] (eV)	-1.39±0.02	0	0.7±0.1	3±1	5.1±0.4	6.9±0.1
Area (arb.)	3920±80	16900±200	2400±300	60±70	500±100	700±100
Atom Assignment	<u>CF</u> ₃ , -O- <u>CF</u> ₂ -CF-O, -O- <u>CF</u> ₂ - <u>CF</u> ₂ -	<u>CF</u> ₂ -CF ₂ -, <u>CF</u> ₂ -CF-O	-O- <u>CF</u> -CF ₃ , CF ₂ - <u>CF</u> -O, S- <u>CF</u> ₂	partially fluorinated carbon	unsaturated, partially fluorinated carbon	graphitic carbon
at%	16.0±0.6	69±3	10±1	0.2±0.3	2.0±0.8	2.9±0.4
Predicted at%	14	71	14			
Width (eV)	1.46±0.04	0.960±0.008	1.40±0.05	0.6±0.4	2.1±0.6	1.3±0.1

The cleavage of the ether group leaves an additional question: What does the oxygen rebond to? Our analysis in Table S4 shows that the oxygen ether peak has both shifted and narrowed, but only slightly. This suggests that some of the ethers have changed from a CF-O-CF₂ configuration prior to EBL to something that still at least has a CF-O group afterwards. However, given the very slight shift, the chemistry is unlikely to be massively changed. One possibility is that the oxygen has formed a new CF-O-CF bond, potentially with a site in the Nafion backbone leading to crosslinking. If such cross linking does happen this will also lead to insolubility of the polymer.

Considering all the above, at minimum we can infer cleavage of ether bonds in the pendant groups, which would decrease the solubility of the polymer in a polar solvent, consistent with what we observe. If this cleavage also leads to crosslinking to an adjacent but separate Nafion backbone, this will only enhance the insolubility.

Notably, the pendant groups remain within the polymer matrix, as indicated by the conservation of atomic percentages in Tables S1-S3 and the lack of massive change in S2p signal in Figure S4.

The sulphur and corresponding oxygen-sulfonate peaks also indicate that the sulfonate groups remain intact and have not reacted. Thus, the species responsible for generating proton current in Nafion is unaffected and thus the proton concentration should be minimally affected by the EBL process. Note however that the proton mobility may change since the morphology has been changed. This is an aspect of EBL processed Nafion that we will discuss in a separate, more detailed study elsewhere.

Table S6. Summary of the results of the fits (relative to the baselines) for the carbon peaks of the EBL sample in Figure S6B. The CF₂ peak was fixed allowing the relative shift of the other peaks to be determined. The predicted *at%* are values obtained from the control sample. The carbons in bold underline are the assigned carbons for that particular peak.

Peak	1	2	3	4	5	6
BE (eV)	292.94±0.02	291.54	290.9±0.1	288.8±0.5	286.40±0.04	284.9±0.5
BE relative to peak 2 [BE _{rp}] (eV)	-1.4±0.02	0	0.6±0.1	2.7±0.5	5.14±0.04	6.6±0.5
Area (arb.)	2600±100	13950±60	2500±200	200±100	1600±500	700±100
Atom Assignment	<u>CF</u> ₃ , -O- <u>CF</u> ₂ -CF-O, -O- <u>CF</u> ₂ -CF ₂ -	<u>CF</u> ₂ -CF ₂ , <u>CF</u> ₂ -CF-O	-O- <u>CF</u> -CF ₃ , CF ₂ - <u>CF</u> -O, S- <u>CF</u> ₂	partially fluorinated carbon	unsaturated, partially fluorinated carbon	graphitic carbon
<i>at%</i>	12.1±0.8	65±3	12±1	0.9±0.5	7±2	3.2±0.5
Predicted <i>at%</i>	16.0	69	10	-	-	-
Width (eV)	1.39±0.04	0.96	1.86±0.09	0.8±0.2	1.25±0.07	1.49±0.07

Table S7. The difference between the various peak parameters of the control and EBL samples in Tables S5 and S6. Data indicates a difference between the ether peaks of the two samples.

Peak	1	2	3	4	5	6
ΔBE _{rp} (eV)	0.01±0.04	-	0.1±0.2	0.3±2	0.04±0.4	0.3±0.6
Δ <i>at%</i>	3.9±1.4	4±6	2±2	0.7±0.8	5±3	0.3±0.9
ΔWidth (eV)	0.07±0.08	-	0.5±0.1	0.2±0.6	0.9±0.7	0.2±0.2

Change in Nafion solubility resulting from thermal annealing

An alternative explanation for the solubility contrast of the Nafion film would be that it is caused by structural changes arising from local heating during the EBL exposure rather than from direct interaction with energetic electrons. Note that this cannot be caused by a global heating process alone or there would be no patterned solubility contrast it must be local heating during the EBL process, however, we can test this possibility using a global heating approach as follows.

Nafion thin films (~230 nm) were spin-coated on Si/SiO₂ substrates at 3000 rpm for 30 s with a 1000 rpm/s ramp. The films were then baked on a hotplate under ambient conditions at different temperatures and durations. Samples were then submerged in a 1:1 2-propanol:acetone developer solution for 1 min to see whether the Nafion films remained soluble. Optical microscopy images were obtained after each step in the process to comprehensively document the state of the film. Figure S7 summarizes the results of the experiments.

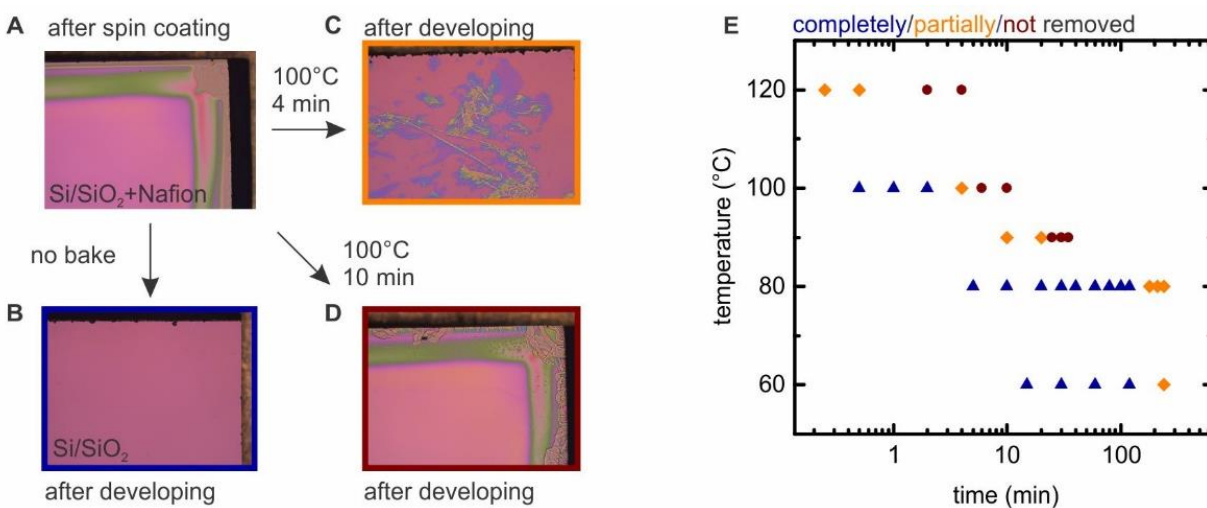


Figure S7. Optical microscopy images of (A) a ~230 nm Nafion film spin-coated on a Si/SiO₂ substrate. (B) The Nafion film is removed completely after the sample is submerged in 1:1 2-propanol:acetone developer for 1 min. (C) The film is only partially removed if the sample is baked for 4 min at 100°C prior to exposure to the developer. (D) A Nafion film baked for 10 min at 100°C was not removed at all. (E) Observed condition of the film after submersion in the developer for different bake temperature and time. The point colour indicates solubility with: (blue) Nafion film completely removed, (orange) partially removed, and (red) not removed.

Figure S7A shows an optical microscopy image of a Nafion film immediately after spin-coating. The colour changes near the edges of the substrate originate from the inhomogeneous thickness of the spin coated Nafion film due to edge effects during spin coating. If the unbaked sample is submerged in the developer solution for 1 min, it is completely removed (see Fig. S7B). Our EBL patterning process relies on this mechanism to remove all the unexposed Nafion.

If the film is baked for 4 min at 100°C then the film is only partially removed (see Fig. S7C). The film becomes insoluble after a 10 min bake at 100°C. This latter bake is a significant finding because to maintain the effectiveness of the developer solution in generating contrast care needs to be taken to avoid exposing the film to high temperatures for extended periods prior to development.

Figure S7E shows the outcome of different bake temperatures and times. Films that were completely removed are shown in blue, partially removed in orange, and not removed in red. Resistance to the developer can be achieved at $\geq 100^\circ\text{C}$ after ~ 6 min. The time required to achieve insolubility increases as the bake temperature is reduced, for example, after 4 hours at 60°C we can still achieve partial removal of the film using the developer solution.

We now compare the conditions expected for the EBL process to the bake temperature and time requirements established above. Local heating in the EBL process is very difficult to measure, however previous work for conventional EBL resists, i.e., ZEP 7000, indicates that it is typically of the order of tens of degrees.⁶ The exposure time for a typical Nafion gate structure in one of our devices is of order seconds and is composed of a raster-scan of individual exposure points each of which lasts $\sim 3 \mu\text{s}$. On this basis, we believe it to be unlikely that the resulting heating is sufficient to cause the changes in solubility observed in the hotplate experiment or produce the required solubility contrast for patterning without associated chemical changes in the Nafion. That said, it is possible that significantly higher temperatures are achieved on the nanoscale. We are currently investigating the impact of electron-beam induced local heating on Nafion and will report on it in a future publication.

Nafion can etch nanowires connected to metal

Initial attempts to make Nafion-gated nanowire field-effect-transistors (NWFETs) followed the fabrication process developed by Carrad *et al.*⁷ for poly(ethylene oxide)-gated NWFETs. This involved creating ohmic contacts to the nanowires prior to spin-coating the polymer electrolyte to create the gates. This was not possible for Nafion because InAs nanowires connected to metal contacts were etched upon Nafion application. Figure S8 shows scanning electron microscope

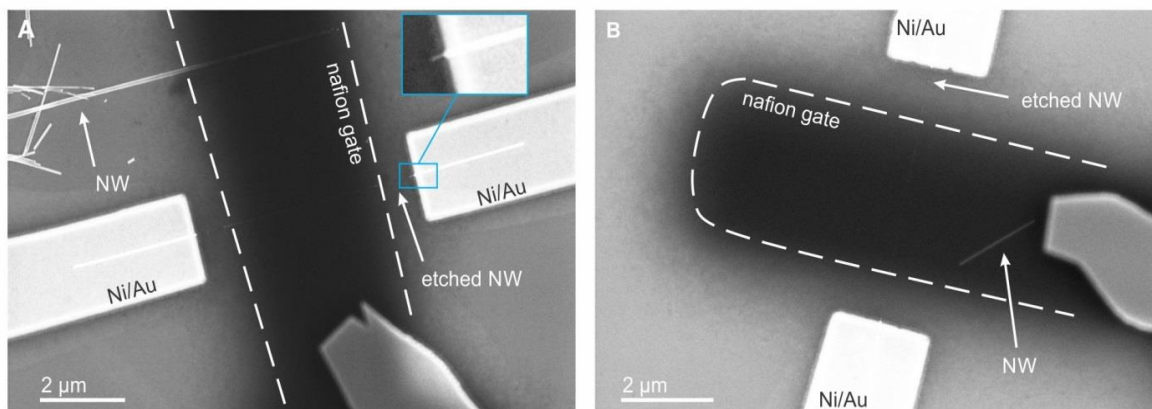


Figure S8 SEM image of two Nafion-gated InAs-NWFETs where the Nafion gate was created after the ohmic contacts. Note that the contacted nanowire was nearly completely etched, whereas (A) Nanowires (NW) with no metal contacts remain relatively intact, (B) even if they are located underneath the patterned Nafion gate.

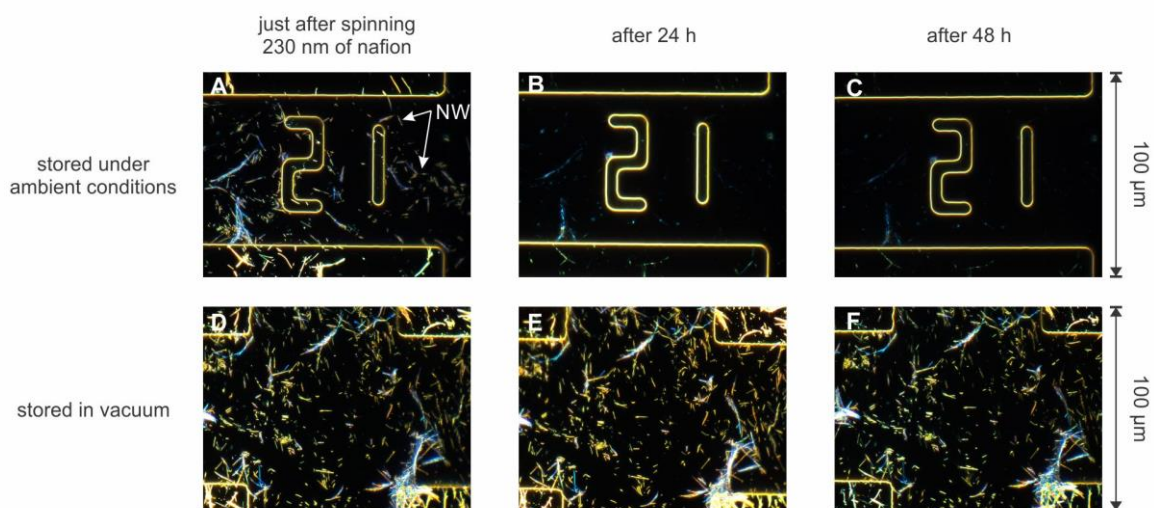


Figure S9 InAs nanowires dispersed on a device substrate spin-coated with Nafion and stored under ambient conditions and vacuum. Optical microscopy dark-field images of a sample stored in ambient conditions (A) immediately after spin coating, (B) 24 hours, (C) and 48 hours after spin coating. Images of a sample stored in vacuum (D) immediately after spin coating, (E) 24 hours and (F) 48 hours after spin coating.

(SEM) images of two devices fabricated in this way. The Nafion gate appears black due to high charge absorption. Both contacted nanowires were removed nearly completely. Other nanowires that were not in contact with metal remained relatively intact. This is true even for nanowires located under the patterned Nafion gate as shown in Figure S8B. This is likely due to metal assisted

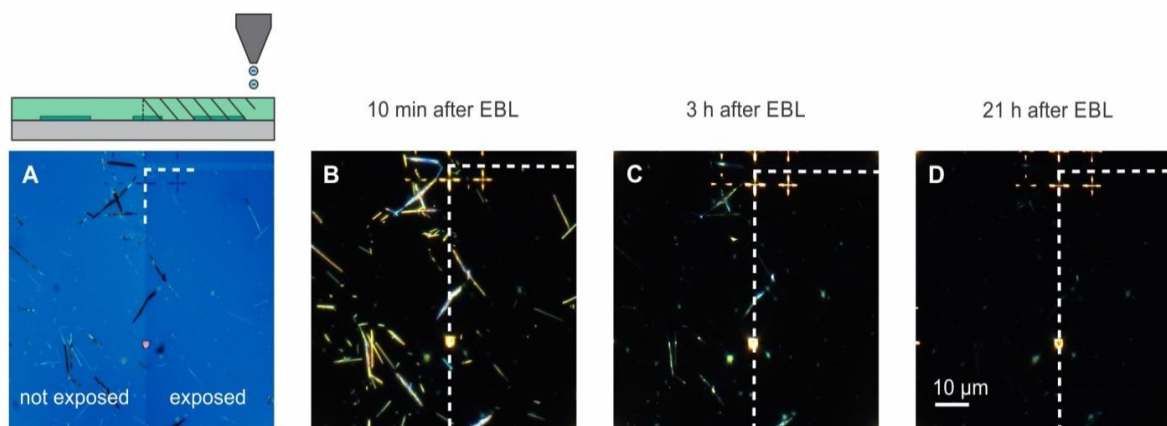


Figure S10 InAs nanowires dispersed on a device substrate and spin-coated with Nafion prior to exposing half of the shown area with an electron beam. (A) optical microscopy bright-field image of a device substrate with nanowires coated with 230 nm of Nafion. The area in the right half of the image was exposed to an electron beam. (B) Dark-field image of the same substrate 10 min, (C) 3 hours, and (D) 21 hours after the EBL exposure.

etching.⁸ This problem can be circumvented by patterning the Nafion gates first, avoiding temporary intersections of Nafion, InAs, and metal as shown in the main text.

We did several tests to better understand the conditions under which the Nafion etches the nanowires and to manage this problem in our device processing. We have already seen that contacted nanowires are rapidly etched. Figure S9A-C show dark-field microscopy images of InAs nanowires distributed on a Si/SiO₂ substrate with some metal structures. The substrate was spin-coated with Nafion and imaged just after spin-coating, 24, and 48 hours later. In between it was stored under ambient conditions. After 24 hours most of the nanowires were removed completely. This shows that Nafion also etches nanowires with no metal contacts; however, this process appears to be slower. We found that the etching can be delayed or slowed down significantly by storing the samples in vacuum or a dry nitrogen atmosphere. Figure S9D-F show images of a similar sample stored in vacuum. No significant etching was observed after 48 hours. The same was true for samples stored in dry nitrogen. This indicates that the etch is dependent on humidity and/or oxygen that is adsorbed into the Nafion films.

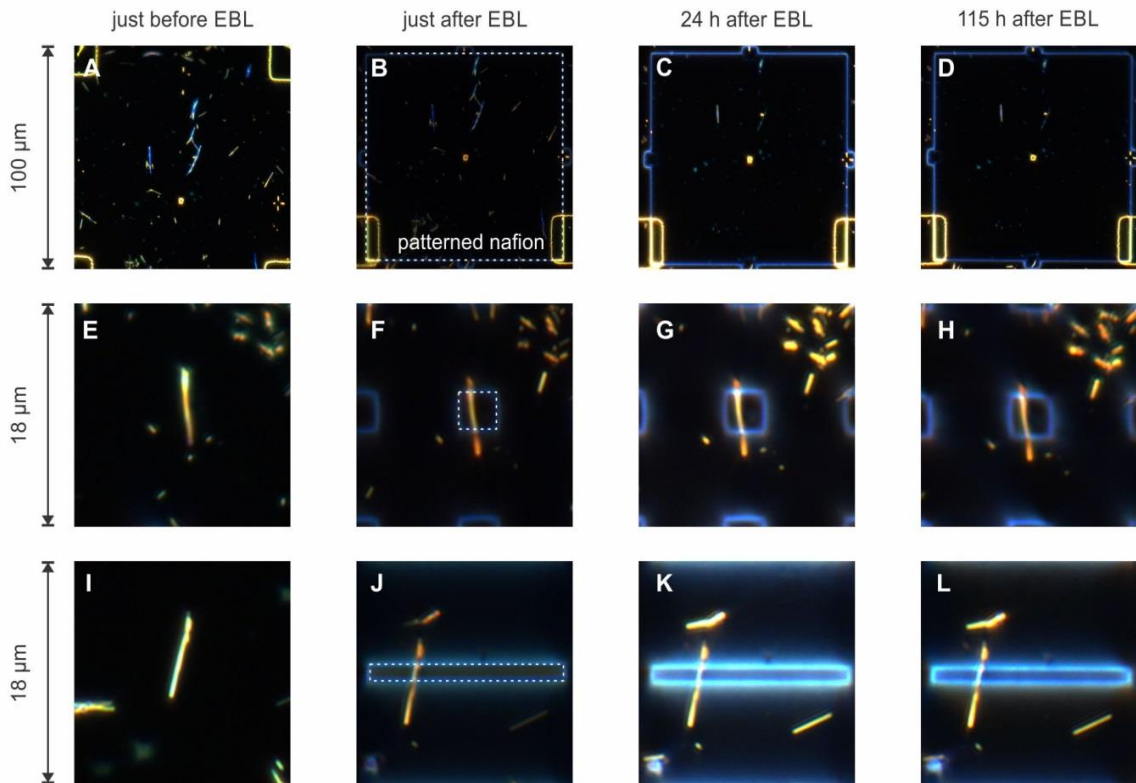


Figure S11 Patterned Nafion structures of different sizes overlapping with InAs nanowires. Optical dark-field images of nanowires dispersed on a device substrate and spin coated with Nafion (A,E,I). Select areas, indicated by dotted lines, were exposed to an electron beam before the sample was developed in 1:1 IPA:acetone. The samples were imaged (B,F,J) just after development, (C,G,K) 24 hours after development, and (D,H,L) 115 hours after development.

Interestingly, Nafion-gated NWFET devices, that were fabricated as outlined in the main text, did not break down due to etching on such short time scales. We tested whether the crosslinking during

the EBL exposure slows down the etch. Figure S10 shows a sample where the right half was exposed to an electron beam (10 kV, 10 μm , 10 $\mu\text{C}/\text{cm}^2$). There is no noticeable difference in etch rate between the exposed and unexposed halves.

In another study we patterned the Nafion to see if the etch is impeded by reducing the size of the Nafion reservoir. Figure S11 shows three areas with Nafion coatings just prior to EBL exposure, just after development, and after 24 and 115 hours. Significant etching of nanowires is still observed for the $90 \times 90 \mu\text{m}^2$ shown in Figure S11A-D. The smaller structures in Figure S11E-H and I-L, on the other hand, showed no obvious sign of etching even after 115 hours. This indicates that the etch can be impeded by reducing the size of the Nafion reservoir interacting with the nanowire. This is consistent with the apparent resilience of the NWFET devices where the Nafion gates are generally only $\sim 2 \mu\text{m}$ wide and a few μm long.

Electrical characterization of a single InAs nanowire transistor with a Nafion gate

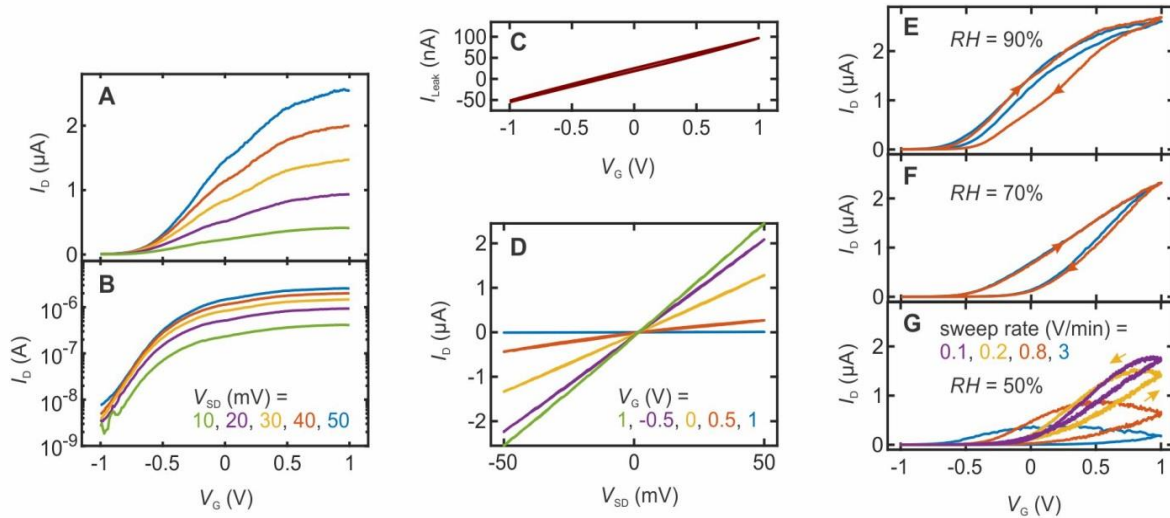


Figure S12 Transfer characteristics of a single *n*-type InAs nanowire field effect transistor with an electron beam-patterned Nafion gate. Drain current I_D vs gate voltage V_G at different source-drain voltages V_{SD} (A) on a linear and (B) logarithmic scale. (C) Gate leakage current to ground. (D) I_D vs V_{SD} at different V_G . I_D vs V_G measured at different gate voltage sweep rates at relative humidities (E) $RH = 90\%$, (F) $RH = 70\%$ and (G) $RH = 50\%$.

Figure S12A/B show drain current I_D vs gate voltage V_G at different source-drain voltages V_{SD} for a single InAs nanowire field effect transistor with an electron beam patterned Nafion gate on a linear and logarithmic scale. All measurements were obtained at a relative humidity RH of around 90% unless otherwise indicated. This device has a subthreshold swing of 270 mV/dec and an on/off ratio of 800 at a source-drain bias $V_{SD} = 50$ mV. A maximum gate leakage current I_{leak} to ground of 100 nA was measured (Figure S12C). The leakage is likely due to moisture adsorbed to the device and decreases significantly with relative humidity. Figure S12D shows that I_D vs V_{SD} is linear across the applied gate voltage range indicating good ohmic contacts to the InAs nanowire.

The hysteresis curves at different relative humidity's are shown in Figure S12E-G. At high RH , I_D vs V_G generally exhibits a moderate clockwise hysteresis comparable to InAs nanowire field effect transistors with oxide or polymer dielectrics.⁹ Hysteresis in InAs nanowire field-effect transistors is generally attributed charge traps at the InAs surface.^{10,11} At 90% and 70% RH , the hysteresis is smaller for a high sweep rate. This is attributed to the change in gate voltage outpacing the population and depopulation of charge traps. At 50% RH a different behavior is observed. The hysteresis loop runs counterclockwise and hysteresis increases with sweep rate. Also note, that *gate action* increases significantly for slower sweep rates. This indicates that the sweep rate dependence may be dominated by the low ionic conductance of the Nafion at low RH .

Additional data from Nafion-gated inverter devices

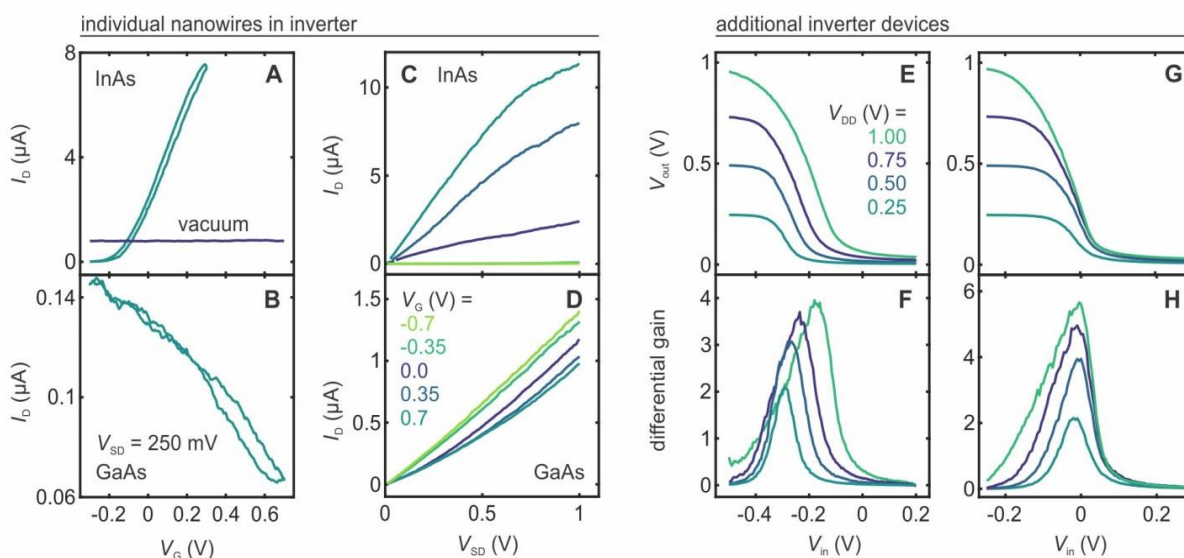


Figure S13 Electrical characteristics of individual nanowires used in an inverter device and electrical data from two additional inverter devices. (A,B) I_D vs V_G and (C,D) I_D vs V_{SD} for the InAs and GaAs nanowires used in the inverter device presented in Fig. 3 of the main text. (E-H) Output characteristics of two additional inverters. All measurements were obtained at a relative humidity RH of around 90-96%.

Figure S13A-D show data from the individual nanowires used in the device characterized in Fig. 3 of the main text. The single InAs nanowire shows strong gating at high relative humidities (green) while no gating action is observed at vacuum (blue) as shown in Figure S13A. For the GaAs nanowire I_D decreases with increasing V_G indicating p -type transport (see Figure S13B). The gating action is not as pronounced as in the InAs. This is expected due to the GaAs nanowire's high carrier concentration chosen for good ohmic contact formation.¹² The high carrier concentration screens external electric fields to the point where no significant gating action can be achieved with traditional oxide-insulated metal gates.¹³ However, electric double-layer formation in polymer electrolyte gates provides stronger gate coupling enabling effective modulation of carrier concentration. Near thermal limit subthreshold slopes in these nanowires have been reported using poly(ethylene oxide) gates.¹³ However, the high carrier concentration is still

associated with threshold voltages of several volts.¹³ We did not access this gate voltage regime because the Nafion inverters operate in a high-humidity environment and voltages over 1.2 V would cause electrolysis. Reducing the carrier concentration in the gated segment while maintaining a high carrier density at the contacts may lead to a reduction of threshold voltage and an increase in device performance. However, axial control over dopant concentration is notoriously hard to achieve in GaAs nanowires during growth¹². Ullah *et al.*¹⁴ recently presented an approach using EBL-patterned wet etching to locally remove the highly doped nanowire shell. This approach may be applicable to future generations of Nafion-gated devices to further increase device performance but would entail careful management of the local thinning etch related to the superacid nature of Nafion when added to the thinned nanowires. This would entail a long, detailed study with a large parameter space regarding the thinning etch and the patterning/handling of the subsequent Nafion gate structure.

Figure S13C/D show the I_D vs V_{SD} for the InAs and GaAs nanowires respectively. The IV curves are approximately linear, with the InAs nanowire showing typical saturation behavior.

Figure S13E-H show data from two additional inverter devices. Both devices achieve effective switching of the output voltage V_{out} with input voltage V_{in} at different supply voltages V_{DD} yielding DC gains of up to 3.9 and 5.7.

References

- 1 E. A. Hoffmann, Z. A. Fekete, L. S. Korugic-Karasz, F. E. Karasz and E. Wilusz, *J. Polym. Sci. Part Polym. Chem.*, 2004, **42**, 551–556.
- 2 G. Beamson and D. Briggs, *High Resolution XPS of Organic Polymers: The Scienta ESCA300 Database*, Wiley, 1992.
- 3 K. A. Mauritz and R. B. Moore, *Chem. Rev.*, 2004, **104**, 4535–4586.
- 4 M. M. Nasef, H. Saidi, H. M. Nor and M. A. Yarmo, *J. Appl. Polym. Sci.*, 2000, **76**, 336–349.
- 5 L. J. Hobson, H. Ozu, M. Yamaguchi, M. Muramatsu and S. Hayase, *J. Mater. Chem.*, 2002, **12**, 1650–1656.
- 6 H. J. Levinson, *Principles of Lithography*, SPIE Press, Bellingham, WA, 2nd edn., 2005.
- 7 D. J. Carrad, A. M. Burke, R. W. Lyttleton, H. J. Joyce, H. H. Tan, C. Jagadish, K. Storm, H. Linke, L. Samuelson and A. P. Micolich, *Nano Lett.*, 2014, **14**, 94–100.
- 8 G. Fülöp, S. d’Hollozy, L. Hofstetter, A. Baumgartner, J. Nygård, C. Schönenberger and S. Csonka, *Nanotechnology*, 2016, **27**, 195303.
- 9 J. G. Gluschke, J. Seidl, R. W. Lyttleton, D. J. Carrad, J. W. Cochrane, S. Lehmann, L. Samuelson and A. P. Micolich, *Nano Lett.*, 2018, **18**, 4431–4439.
- 10 G. W. Holloway, Y. Song, C. M. Haapamaki, R. R. LaPierre and J. Baugh, *J. Appl. Phys.*, 2013, **113**, 024511.
- 11 D. Lynall, S. V. Nair, D. Gutstein, A. Shik, I. G. Savelyev, M. Blumin and H. E. Ruda, *Nano Lett.*, 2018, **18**, 1387–1395.
- 12 A. R. Ullah, J. G. Gluschke, P. Krogstrup, C. B. Sørensen, J. Nygård and A. P. Micolich, *Nanotechnology*, 2017, **28**, 134005.
- 13 A. R. Ullah, D. J. Carrad, P. Krogstrup, J. Nygård and A. P. Micolich, *Phys. Rev. Mater.*, 2018, **2**, 025601.
- 14 A. R. Ullah, F. Meyer, J. G. Gluschke, S. Naureen, P. Caroff, P. Krogstrup, J. Nygård and A. P. Micolich, *Nano Lett.*, 2018, **18**, 5673–5680.